Energy & Environmental Science

Surface Decoration Accelerates Hydrogen Evolution Kinetics of Perovskite Oxide in Alkaline Solution

Journal:	*Energy & Environmental Science*
Manuscript ID	EE-ART-05-2020-001598.R2
Article Type:	Paper
Date Submitted by the Author:	01-Sep-2020
Complete List of Authors:	Hu, Chun; Shanghai Institute of Ceramics Chinese Academy of Sciences, State Key Laboratory of High Performance Ceramics and Superfine Microstructure Hong, Jinghua; National Institute of Advanced Industrial Science and Technology Huang, Jian; Shanghai Institute of Ceramics Chinese Academy of Sciences, State Key Laboratory of High Performance Ceramics and Superfine Microstructure Chen, Wei; E O Lawrence Berkeley National Laboratory, Segre, Carlo; Illinois Institute of Technology, Physics & CSRRI Suenaga, Kazu; National Institute of Advanced Industrial Science and Technology Zhao, Wei; Shanghai Institute of Ceramics, Chinese Academy of Sciences Huang, Fu Qiang; Shanghai Institute of Ceramics Chinese Academy of Sciences, Wang, Jiacheng; Shanghai Institute of Ceramics, State Key Laboratory of High Performance Ceramics and Superfine Microstructure

Energy & Environmental Science

ARTICLE

Surface Decoration Accelerates Hydrogen Evolution Kinetics of Perovskite Oxide in Alkaline Solution

Chun Hu,[a,c,g] Jinhua Hong,[f,g] Jian Huang,*[a,b] Wei Chen,[d] Carlo U. Segre,[e] Kazu Suenaga,[f] Wei Zhao,[a] Fuqiang Huang*[a,b] and Jiacheng Wang*[a,b]

Received 00th January 20xx,
Accepted 00th January 20xx

DOI: 10.1039/x0xx00000x

As an important class of inorganic compounds that exhibit a variety of physical, chemical, and electrochemical properties, $ABO_{3\pm\delta}$ perovskites are generally known as active electrocatalysts for the anodic oxygen evolution reaction (OER). However, the inferior performance for the cathodic hydrogen evolution reaction (HER) limits their wide potential in constructing stable oxide-based alkaline electrolyzer for hydrogen production. Here, we show the efficient decoration of perovskite oxide $(K_{0.469}La_{0.531})TiO_3$ (KLTO) *via* surface ion exchange with Ru cations and nucleation growth of Ti-doped RuO_2 (TRO) nanoparticles could form a composite oxide-type electrocatalyst. It enables fast water dissociation with excellent HER activity in alkaline solution, superior to other oxide electrocatalysts and commercial Pt/C. Theoretical and experimental studies imply that the co-existence of surface TRO nanoparticles and Ru-doped KLTO (RKLTO) substrate synergistically enhances alkaline hydrogen evolution kinetics. Ti doping into RuO_2 lattice could significantly reduce the barrier of water dissociation to facilitate the Volmer process. And the surface doping of Ru in the KLTO substrate could regulate and optimize the hydrogen adsorption free energy. The present strategy represents a new concept for designing oxides-based electrocatalysts related to the devices of energy conversion and storage.

Introduction

As a large and important class of functional materials, the perovskite metal oxides $ABO_{3\pm\delta}$, where A is a rare-earth or alkaline earth element, and B is a transition metal, have attracted great interest in microelectronic, optoelectronic, and electrochemical fields owing to their high structural and compositional flexibility, and unique physicochemical properties.[1-5] The ability to accommodate doping ions with different size, valence and electronegativity in both A and B sites makes it an ideal target for analysing the connections between composition, crystal/electronic structure and functional performance, especially in catalytic applications.[6, 7] The perovskite oxides have been well studied as the water splitting electrocatalysts, and have achieved high-performance for oxygen evolution reaction (OER) by chemical substitution, defects/interface engineering, lattice strain modulation, *etc*.[8-16] Thereinto, most studies are motivated by the molecular orbital principles that affect catalysis, including the filling of e_g orbital,[3, 17] the number of *d* electrons,[18] hybridization between metal 3*d* and oxygen 2*p*,[19] the charge transfer energy,[20] *etc*.

For HER, pure transition metal oxides involving perovskites generally exhibit poor electrocatalytic HER activity, and even ruthenium dioxide (RuO_2), which is always regarded as the state-of-the-art OER catalyst, is no exception.[21-23] Nevertheless, a few metal oxides, such as $(Gd_{0.5}La_{0.5})BaCo_2O_{5.5+\delta}$,[24] CoO nanorods,[25] $Pr_{0.5}(Ba_{0.5}Sr_{0.5})_{0.5}Co_{0.8}Fe_{0.2}O_{3-\delta}$,[26] and $SrNb_{0.1}Co_{0.7}Fe_{0.2}O_{3-\delta}$,[27] have been proved to exhibit considerable HER activities. However, the origin of the HER electrocatalytic activity with the oxide's inherent characteristics is unclear, and there is no established criterion for constructing highly efficient perovskites catalysts for HER.

In this work, we modify the surface composition and structure of perovskite oxide $K_{0.469}La_{0.531}TiO_3$ (KLTO) by simple hydrothermal treatment with an $RuCl_3$ solution to obtain a high-activity oxide-type electrocatalyst for alkaline HER. Advanced characterization techniques imply the surface doping of Ru *via* the ion exchange to form Ru-doped KLTO (RKLTO) as well as the nucleation growth of Ti-doped RuO_2 (TRO) nanoparticles on the surface during the hydrothermal treatment. The resulting TRO/RKLTO exhibits remarkable hydrogen evolution activity with a low overpotential (η_{10} = 20 mV vs. reversible hydrogen electrode (RHE), high mass activity (320 A g_{Ru}^{-1}) and price activity (39 A dollar^{-1}) at an overpotential of 0.05 V in 1 M KOH, surpassing other state-of the-art oxide electrocatalysts, and even superior to that of commercial RuO_2 and Pt/C. Density functional theory (DFT) calculations reveal that fast water dissociation on TRO nanoparticles and optimal hydrogen binding on RKLTO synergistically enhance HER performance in an alkaline environment.

[a] State Key Laboratory of High Performance Ceramics and Superfine Microstructure, Shanghai Institute of Ceramics, Chinese Academy of Sciences, Shanghai 200050, China. E-mail: jhuang@mail.sic.ac.cn, huangfq@mail.sic.ac.cn, jiacheng.wang@mail.sic.ac.cn
[b] Center of Materials Science and Optoelectronics Engineering, University of Chinese Academy of Sciences, Beijing 100049, China.
[c] University of the Chinese Academy of Sciences, Beijing 100049, China.
[d] Department of Mechanical, Materials and Aerospace Engineering, Illinois Institute of Technology, Chicago, IL 60616, USA
[e] Department of Physics & Center for Synchrotron Radiation Research and Instrumentation, Illinois Institute of Technology, Chicago, IL 60616, USA
[f] Nanomaterials Research Institute, National Institute of Advanced Industrial Science and Technology (AIST), Tsukuba 305-8565, Japan.
[g] These authors contribute equally.
†Electronic Supplementary Information (ESI) available: See DOI: 10.1039/x0xx00000x

Experimental

Materials synthesis

The $K_{0.469}La_{0.531}TiO_3$ (KLTO) substrate was synthesized by a hydrothermal process according to our previously reported method.[28] Briefly, 3 mmol $Ti(SO_4)_2$ and 2 mmol $La(NO_3)_3{\cdot}6H_2O$ were added into 20 mL of 8 M KOH solution, which was then magnetically stirred for 2 h to obtain a white suspension. Subsequently, the white suspension was transferred to a Teflon-lined autoclave, sealed, and heated at 200 °C for 20 h. The white product was filtered and washed with 0.1 M dilute hydrochloric acid to remove undesired $La(OH)_3$ species. The product was rinsed with deionized water and ethyl alcohol, and dried in an oven at 60 °C overnight. Finally, the resulting product was ground to a fine powder for further use. For the preparation of TRO/RKLTO catalyst, 0.48 mmol (0.1g) $RuCl_3{\cdot}xH_2O$ was dissolved in deionized water to form a homogeneous solution (pH=1~2). Then, the appropriate amount of as-prepared KLTO was added into above solution and stirred for 30 min. The resulting mixture was transferred to a Teflon-lined autoclave and placed in an oven at 120 °C for 12 h. The precipitate was collected and washed with deionized water for several times, then dried under vacuum at 60 °C for 12 h. In order to investigate the role of Ru loading, the TRO/RKLTO-x with differing Ru amounts (x=0.01, 0.03, 0.05, 0.2 g) were prepared as well. For comparison, RuO_2 and KLTO were dispersed in deionized water, while concentrated hydrochloric acid was employed to adjust pH value (1~2). And the obtained sample was marked as RuO_2/KLTO.

Structural characterization

X-ray power diffraction patterns were obtained with a Bruker D8 advance diffractometer operating with Cu Kα radiation (λ=0.15404 nm). The surface morphology was measured by scanning electron microscopy (SEM, JEOL S-4800). TEM and HRTEM images were recorded on JEOL-JEM 2100F transmission electron microscope (TEM), operating at an accelerating voltage of 200 kV. The Cs-corrected TEM images were collected on JEOL JEM-2100CF (triple C1, delta corrector, operating voltage: 60 kV). The N_2 adsorption-desorption measurements were performed using Quadrasorb SI surface area and pore size analyser (Quantachrome Ins) at 77 K. X-ray photoelectron spectroscopy was carried out on an AXIS Ultra DLD instruments (Shimadzu/KRATOS, UK), using a monochromatic Al Kα radiation source and the C1s peak at 284.8 eV as calibrated standard. The Ru content of the catalysts was measured by inductively coupled plasma atomic emission spectroscopy (ICP-AES) using iCAP 6300 spectrometer. To measure the amount of metal dissolution in the 1 M KOH solution, the supernatant (10 mL) of electrolyte after stability test was taken for ICP-OES measurement. XAS data were collected at the Materials Research Collaborative Access Team (MRCAT), Sector 10-BM of the Advanced Photon Source at Argonne National Laboratory. The samples were mixed with boron nitride and PVDF then pressed into a pellet and enclosed in Kapton tape and measured in fluorescence mode with a 4-element Vortex SDD (Hitachi) K-edge absorption of Ti (4.97 keV) and Ru (22.10 keV). Metal foils of either Ti or Ru were used to calibrate the monochromator energy and served as reference material for determination of S_0^2 values used in subsequent EXAFS fits. All data were corrected for self-absorption. Processing and fitting of data were performed using the Athena and Artemis programs from the IFEFFIT suite.[29, 30]

Electrochemical measurements

The electrocatalytic performance in 1M KOH alkaline solution was evaluated on the CHI760E electrochemical station in a three-electrode electrochemical cell (Pine Research Instrumentation). A glassy carbon electrode (GC, 5.0 mm in diameter), an Hg/HgO electrode, and a carbon rod were employed as the working electrode, reference electrode, and counter electrode, respectively. And the Hg/HgO electrode was experimentally calibrated against RHE. The working electrodes were prepared by controlled drop cast catalyst inks onto GC electrode, which was pre-polished with alumina slurry. To eliminate the influence of electrode conductivity within thin film working electrodes, the catalysts were mixed with carbon black (XC72R, Vulcan). Briefly, 5 mg of the as-synthesized catalysts and 2 mg of carbon black (XC72R, Vulcan) were dispersed in 0.5 ml of solvent (0.25 mL alcohol and 0.25 mL deionized water) with 25 µl of Nafion solution (Aldrich, 5%) to obtain a homogeneous catalyst ink. Then, 10 µL of the suspension was dropped onto a glassy carbon electrode and dried in ambient conditions. The catalyst loading on the working electrode was about 0.485 mg cm^{-2}. In addition, the commercial Pt/C (Johnson Matthey, 20 wt.%) and RuO_2 (Macklin, 99.9% metals basis) catalysts with the identical loading amount were used for comparison. Before the electrochemical measurement, the working electrode was activated by cyclic voltammograms (CV) at a scan rate of 100 mV s^{-1} between 0 and 1.20 V vs. RHE until stable CV curves were obtained. The linear sweep voltammetry (LSV) polarization curves were carried out from 0.15 to -0.25 V at a scan rate of 2 mV s^{-1}, and all LSV data were presented with IR compensation. The CV was conducted between -0.1 V and 0.1 V at a scan rate of 100 mV s^{-1} for 5000 cycles to investigate the cycling stability, followed by chronoamperometry to further test the stability. Electrochemical impedance spectroscopy (EIS, -0.05 V vs. RHE) was performed from 1 Hz to 100 kHz at an alternating current voltage amplitude of 10 mV. The electrochemically active surface areas (ECSA) were estimated based on the electrochemical double-layer capacitance of various electrocatalysts at non-faradaic overpotentials. The Tafel slope were obtained from the transformation of polarization curves based on the Tafel equation ($\eta = a + b \log j$, where η is overpotential, a is intercept, b is Tafel slope and j is current density). The hydrogen evolution yields at various time in 1M KOH electrolyte were measured by gas chromatography (7820A, Agilent), and H_2 quantification was detected via a thermal conductivity detector (TCD). And the Faradaic efficiency was evaluated from the linearity of experimental results.

Theoretical calculations

All calculations were performed with DFT using the *Vienna Ab initio Simulation Package* (VASP).[31] A plane-wave basis and projector augmented wave method (PAW) pseudopotentials were used.[32] The Perdew-Burke-Ernzerhof (PBE) generalized gradient approximation (GGA) was adopted to treat exchange-correlation effects.[33] A cut-off of 520 eV was imposed on the planewave kinetic energy. The convergence criterion of the total energy was set to 10^{-7} eV. Atomic and lattice parameter relaxations were optimized by a conjugate-

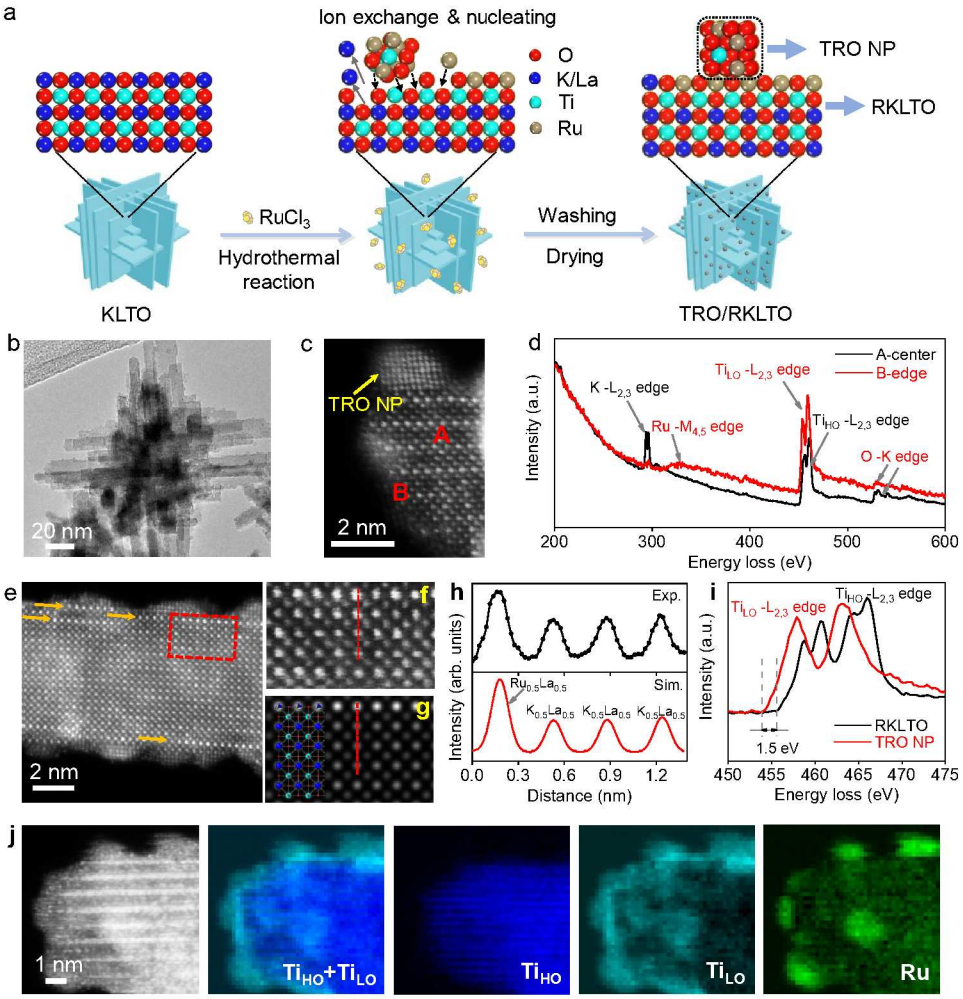

Fig. 1 Synthesis and structural characterization of TRO/RKLTO. a, Schematic illustration of the synthetic process for Ru-doped $K_{0.469}La_{0.531}TiO_3$ supported Ti-doped RuO_2 nanoparticles composite (TRO/RKLTO). b, TEM image of TRO/RKLTO. c, HAADF-STEM image of TRO/RKLTO, demonstrating the crystalline structure of TRO nanoparticle and KLTO substrate. d, EELS spectra of A-center and B-edge in c. e, Experimental ADF-STEM image of the RKLTO substrate. Arrows indicate the enrichment of Ru which replaces K in the surface or edge regions of KLTO. f, Zoom-in experimental image of the part marked by red dashed rectangle in e. g, Simulated ADF-STEM image, where Ru substituting K occurs in the atomic model superimposed. h, Comparison of the experimental and simulated ADF-STEM intensities along the dashed line red in f and g. i, The detailed Ti-EELS profiles. Ti_{HO} and Ti_{LO} represent higher oxidation state (4+) and lower oxidation state (3+) of Ti, respectively. j, HAADF-STEM image and elemental mapping of TRO/RKLTO. The STEM-EELS mapping shows the correlation of Ti_{HO}, Ti_{LO}, and Ru components.

gradient (CG) algorithm with an imposed numerical threshold of 0.005 eV/Å. We also considered the van der Waals interaction in the present study using the DFT-D3 method of Grimme.[34] Following the standard procedure,[35] the free energy ΔG_H for hydrogen adsorption is calculated by:

$$\Delta G_H = \Delta E_H + \Delta E_{ZPE} - T\Delta S_H \quad (1)$$

where ΔE_H is the chemisorption energy of hydrogen atom, ΔE_{ZPE} is the correction of zeropoint energy, ΔS_H is the entropy difference between the adsorbed state and the gas state and T is the room temperature (300K herein).

For the study of energy barriers used to determine the kinetic behaviour of water splitting, we employed nudged elastic band (NEB)[36] calculations as developed by Henkelman with eight image structures between the reactant and the product.

Results and discussion

Synthesis and structural characterization

The as-synthesized KLTO forms in the shape of a nanoflower with size of ~100 nm self-assembled by two-dimensional nanosheets (Supplementary Fig. 1). The X-ray diffraction (XRD) pattern of KLTO reveals that all diffraction peaks are consistent with the cubic $(K_{0.469}La_{0.531})TiO_3$ (KLTO, $Pm\bar{3}m$, JCPDS 89-4930) without detectable impurities (Supplementary Fig. 2). In particular, the K/La cations in perovskite KLTO occupy the cavities formed by the corner-linked $[TiO_6]$ octahedral, thus making it more flexible to be replaced by

Energy & Environmental Science

ARTICLE

other cations while still maintaining the original crystal structure as much as possible, compared with the Ti cation. The hydrothermal treatment of KLTO with $RuCl_3$ solution unchanged the flower-like morphology of the KLTO (Fig. 1b), but it could result in surface ion exchange to form Ru-doped KLTO (RKLTO) as well additional nucleation to produce Ti-doped RuO_2 (TRO) nanoparticles on the surface (Fig. 1a). Scanning electron microscopy energy dispersive X-ray spectroscopy (SEM-EDS) confirms the existence of Ru element in the final sample (Supplementary Fig. 3 and Table 1), implying the successful incorporation of Ru into the KLTO matrix. Inductively coupled plasma atomic emission spectroscopy (ICP-AES) measurements indicate 17.42 wt.% of Ru in TRO/RKLTO. High-resolution transmission electron microscopy (HRTEM) measurements show the internal structure of KLTO substrate remains unchanged after hydrothermal treatment with $RuCl_3$ (Supplementary Fig. 4). The atomic arrangements of the TRO nanoparticle and the KLTO substrate are presented in the high-angle annular dark-field scanning transmission electron microscopy (HAADF-STEM) image (Fig. 1c). The TRO nanoparticle grows along the lattice of the KLTO support, and the interplanar spacing could be assigned to the tetragonal RuO_2 (P42/mnm, JCPDS 70-2662). The refined electron energy loss spectroscopy (EELS) spectra extracted from marked A and B regions in Fig. 1c are shown in Fig. 1d. Obviously, a much lower intensity of K-$L_{2,3}$ edge and a significant Ru-$M_{4,5}$ edge in B region demonstrate that the surface K of KLTO substrate is replaced by Ru element. The same result is presented in energy-dispersive X-ray spectroscopy (EDS) mapping. Supplementary Fig. 5 shows the surface of KLTO is K-deficient, and Ru is confined in the surface region. In order to further confirm Ru incorporation state on the surface of KLTO support, we simulated the experimental ADF-STEM image of the TRO/RKLTO. As illustrated in Fig. 1e-g, the fitted image was especially consistent with the experimental result, when all K cations on the surface of KLTO are replaced by Ru. And the significantly enhanced intensity further demonstrates the successful replacement with Ru (Fig. 1h).

The crystal structures of TRO/RKLTO and other control samples were also analysed by X-ray diffraction (XRD), as shown in Supplementary Fig. 4, Fig. 6-7. The peaks related to the KLTO phase can be observed in the XRD spectra of TRO/RKLTO, KLTO and TRO/RKLTO-x (x=0.01, 0.03, 0.05, 0.2). There is no obvious RuO_2 phase in TRO/RKLTO and TRO/RKLTO-x (x=0.01, 0.03, 0.05, 0.2), implying the high dispersion and/or low degree of crystallinity of the Ru-related species. Regarding to RuO_2/KLTO, both of KLTO and RuO_2 phase are detected, revealing the mixture of two phases (Supplementary Fig. 6). The TRO/RKLTO shows a large Brunauer–Emmett–Teller (BET) surface area of 75.4 m^2 g^{-1} (Supplementary Fig. 8 and Fig. 9), originating from the stacking of layered KLTO nanosheets, and this could expose more crystalline planes and accessible catalytic sites.

The refined elemental distribution of the anchored nanoparticles and the substrate were further examined by HAADF-STEM image together with the electron energy loss spectroscopy (EELS) spectra. As illustrated in Supplementary Fig. 10, a wide-range EELS analysis on the substrate confirms the relevant elements. Moreover, the Ti element also exists in the nanoparticles, indicating the co-existence of Ru and Ti. It is noteworthy that the EELS spectrum of Ti in the substrate and nanoparticles are totally different (Fig. 1i). The valence state of Ti in the substrate is +4 (Ti^{4+}), which is determined by charge balance in the KLTO phase. However, the abnormal lower valence state of Ti^{3+} in nanoparticles is notable. The STEM-EELS mapping reveals a dense population of Ti^{3+} (Ti_{LO}: LO means low valence) and Ru in the surface nanoparticles, while Ti^{4+} (Ti_{HO}: HO means high valence) is derived from the substrate. Furthermore, the Ti_{LO} and Ru in the surface nanoparticles are uniformly distributed rather than being segregated (Fig. 1j and Supplementary Fig. 11). Considering that both of RuO_2 and TiO_2 have tetragonal rutile phase and that Ru^{4+} and Ti^{3+} have similar ionic radii, it could be concluded that the oxide nanoparticles are Ti-doped RuO_2 (TRO). Except for surface TRO nanoparticles, Ti_{LO} and Ru are also homogeneously distributed on the substrate surface (Fig. 1j), showing the surface doping of Ru *via* the ion exchange process.

Chemical state and electronic structure

X-ray photoelectron spectroscopy (XPS) and X-ray absorption spectroscopy (XAS) measurements were used to elucidate the valence states and chemical environment of the as-synthesized materials. XPS survey spectra further confirm the presence of K, La, Ti, O and Ru in TRO/RKLTO (Supplementary Fig. 13), which is consistent with the SEM and TEM results. Fig. 2a shows the spectra of the Ru 3*d* core-level regions of TRO/RKLTO and KLTO. The two peaks located at 280.8 and 282.3 eV correspond to Ru^{4+} $3d_{5/2}$ and Ru^{5+} $3d_{5/2}$, respectively, while the other three peaks could be assigned to C 1*s* due to surface carbon contamination.[37, 38] Fig. 2b shows the X-ray absorption near-edge structure (XANES) spectra of TRO/RKLTO, Ru and RuO_2. It is obvious that the absorption edge of TRO/RKLTO is close to that of RuO_2, but different from that of Ru, which is in accordance with the EELS measurements (Fig. 1). The Fourier transform X-ray absorption fine structure (FT-EXAFS) spectrum (non-phase shift corrected) of TRO/RKLTO shows a main peak, which is fitted by a Ru-O shell with a bond distance of 1.99 Å, longer than the 1.96 Å distance in RuO_2. Considering that the ionic radius of Ti^{3+} is larger than that of Ru^{4+}/Ru^{5+}, it is likely that the Ru-O bond length would lengthen when Ti is doped into the RuO_2 lattice. The coordination number (CN) of Ru-O was found to be 3.22, which is much lower than that for RuO_2 (Fig. 2c and Supplementary Table 2). The large decrease of CN is probably ascribed to three factors: the size effect of nanosized particles (high occupancy of surface and corner atoms in nanoparticles),

Energy & Environmental Science

ARTICLE

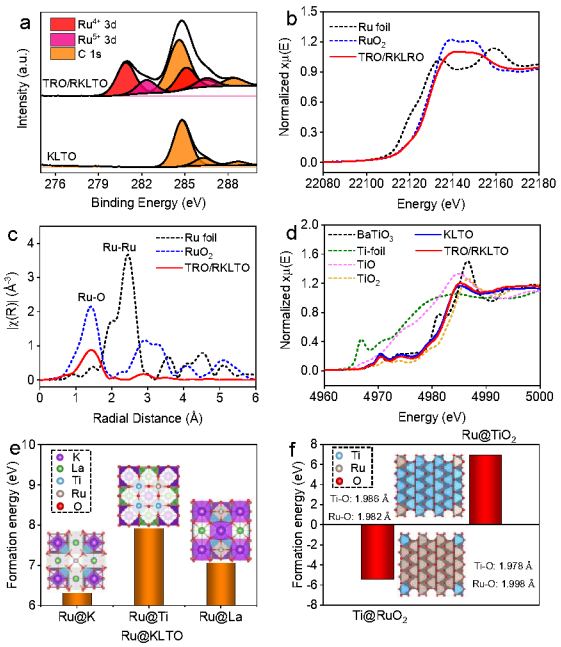

Fig. 2 Oxidation state and structural definition. a, High-resolution Ru 3*d* XPS spectra of KLTO and TRO/RKLTO. b, Ru K-edge XANES spectra of TRO/RKLTO and references. c, Fourier transformed EXAFS k^2-weighted χ(R) function spectra (non-phase shift corrected) of Ru in TRO/RKLTO and references. d, Ti K-edge XANES spectra of TRO/RKLTO and references. Defect formation energies for (e) Ru-doped KLTO and (f) TiO_2/RuO_2 solid solution, and optimized atomic structures are also presented.

abundant doped Ru cations on the surface of KLTO substrate, and oxygen vacancies (normally present in oxides).

The XPS binding energy of 458.4 and 464.1 eV for Ti 2*p* are attributed to $Ti^{4+}2p_{3/2}$ and $Ti^{4+}2p_{1/2}$, respectively, while the additional peak located at ~462.5 eV is derived from Ru 3*p* (Supplementary Fig. 15).[38] Similar results are observed in the XANES spectra. As illustrated in Fig. 2d, the valence state of Ti in TRO/RKLTO is mainly +4, which is identical to that in the bulk KLTO phase. The forbidden quadrupole transitions appearing in the pre-edge region are identical with the perovskite standard, $BaTiO_3$ rather than those of TiO_2. The corresponding FT-EXAFS (non-phase shift corrected) reveals that the Ti-O distances (1.94 Å) in TRO/RKLTO are basically the same as those in $BaTiO_3$ and TiO_2 (Supplementary Fig. 18 and Table 3). These findings suggest that the dominant amount of Ti resides in KLTO (Ti^{4+}) rather than in TRO nanoparticles (Ti^{3+}).

To confirm our experimental results, DFT calculations were carried out by the *Vienna Ab initio Simulation Package* (VASP)[31] while considering the Van der Waals interaction.[39] The defect formation energy for doped system was initially investigated as shown in Fig. 2e-f. For Ru doping into KLTO matrix, it is easier for Ru to settle down at K site with formation energy of 6.54 eV compared to the larger value of 7.17 eV for Ti site and 8.15 eV for La site (Fig. 2e). On the other hand, for the solid solution of TiO_2/RuO_2, Ti doping in RuO_2 (Ti@RuO_2) is much preferred with negative formation energy than the Ru doping in TiO_2 (Ru@TiO_2) (Fig. 2f). Thus, there are likely two forms of Ru in the TRO/RKLTO sample: substituting K cations on the surface of KLTO (Ru@K), and solid solution in TRO (Ti@RuO_2).

Evaluation towards electrochemical hydrogen evolution

The electrochemical activity of TRO/RKLTO was examined using a three-electrode configuration in 1 M KOH electrolyte, employing graphite rod and Hg/HgO electrode as the counter and reference electrodes, respectively. For comparison, RuO_2/KLTO, KLTO, commercial RuO_2 and Pt/C as well as TRO/RKLTO-x (x=0.01, 0.03, 0.05 and 0.2) were also investigated under the same conditions. All potentials were referenced to the reversible hydrogen electrode (RHE). As depicted in Fig. 3a, the KLTO demonstrates a sluggish HER activity over a wide potential range. However, TRO/RKLTO achieves a very low overpotential of 20 mV at a current density of 10 mA cm^{-2} (η_{10}), which is superior to RuO_2/KLTO (91 mV), RuO_2 (101 mV), and even surpasses that of commercial Pt/C. It is also far superior to the other TRO/RKLTO-x catalysts (Supplementary Fig. 23).

In general, HER proceeds via the either Volmer-Heyrovsky or Volmer-Tafel process. And as a rate-determining step for HER, the Tafel slope of Volmer, Heyrovsky and Tafel step is usually defined as 120, 40 and 30 mV dec^{-1}, respectively.[40, 41] Tafel plots were generated from the polarization curves to throw light on the reaction mechanism for the HER process of TRO/RKLTO and the control samples. As illustrated in Fig. 3b, TRO/RKLTO yields a Tafel slope of 30 mV dec^{-1}, which is smaller than Pt/C (34 mV dec^{-1}), RuO_2 (71 mV dec^{-1}), RuO_2/KLTO (72 mV dec^{-1}) and KLTO (126 mV dec^{-1}). This suggests the HER process in TRO/RKLTO mainly follows the Volmer-Tafel mechanism. Thereinto, the recombination of hydrogen adsorbates determines the overall reaction rate.[42-44]

The charge transfer resistance (R_{ct}) during the HER process was further studied by electrochemical impedance spectroscopy (EIS), and it is always reflected in the semicircle in the low frequency range. As shown in Fig. 3c and Supplementary Fig. 23, TRO/RKLTO delivers the smallest R_{ct} among all samples, which indicates the fastest hydrogen evolution kinetics on the TRO/RKLTO catalyst. Moreover, the activity of as-prepared catalysts was further evaluated via electrochemically active surface area (ECSA), which is estimated from the double-layer capacitance (C_{dl}) measurements.[45] As displayed in Supplementary Fig. 25, TRO/RKLTO has the largest C_{dl} value (27 mF cm^{-2}), in contrast to those of Pt/C (11.8 mF cm^{-2}), RuO_2 (19.4 mF cm^{-2}), RuO_2/KLTO (10.2 mF cm^{-2}) and KLTO (1 mF cm^{-2}). The HER activity was further investigated by the Faradaic efficiency measurements. As shown in Supplementary Fig. 26, the detected volume of hydrogen gas well corresponds with the theoretical one, indicating a Faraday efficiency close to 100%.

To assess the electrocatalytic activity of the as-prepared electrocatalysts, it is essential to calculate the specific activity

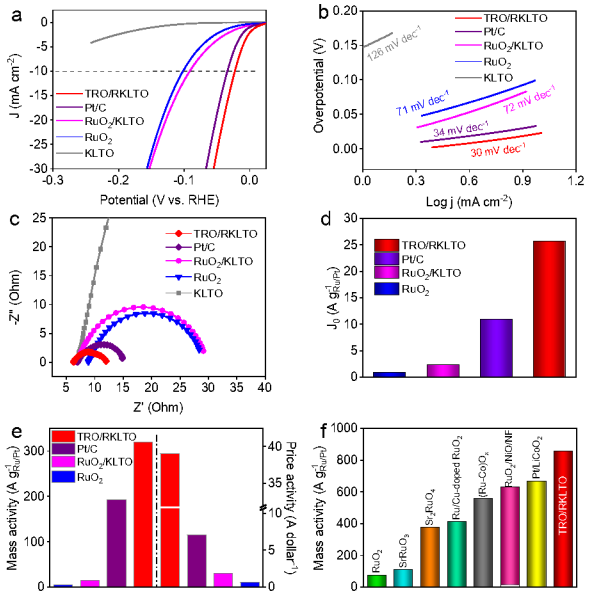

Fig. 3 Electrocatalytic HER performance of TRO/RKLTO and the control samples. a, HER polarization curves and corresponding Tafel plots (b), and Nyquist plots (c) of TRO/RKLTO, Pt/C, RuO_2/KLTO, RuO_2, and KLTO in 1 M KOH solution. d, Exchange current density (J_0) normalized to the mass of Ru/Pt (A $g^{-1}_{Ru/Pt}$) of TRO/RKLTO, Pt/C, RuO_2/KLTO, RuO_2. e, Mass activity and price activity of TRO/RKLTO, Pt/C, RuO_2/KLTO, RuO_2 at the overpotential of η=0.05 V. f, Mass activity of TRO/RKLTO in contrast to the reported oxide-based catalysts.

normalized to the real oxide surface area via BET measurements (Supplementary Fig. 8 and Fig. 9). As illustrated in Supplementary Fig. 27, the specific activity of TRO/RKLTO is still much higher than those of Pt/C, RuO_2/KLTO, RuO_2 and KLTO, when the current densities are normalized by the BET surface area. Moreover, the exchange current density (J_0) was extracted by extrapolating the Tafel plots to zero overpotential, which was normalized to the mass of Ru/Pt (A $g^{-1}_{Ru/Pt}$). The J_0 is closely related to the nature of the catalyst and reflects the kinetic reaction rate between the catalyst and the electrolyte.[46] As shown in Fig. 3d, the J_0 value of TRO/RKLTO is 25.7 A g^{-1}_{Ru}, which is 2.4, 11.2 and 28.6 times that of Pt/C (10.9 A g^{-1}_{Pt}), RuO_2/KLTO (2.3 A g^{-1}_{Ru}) and RuO_2 (0.9 A g^{-1}_{Ru}), respectively.

Fig. 3e shows the comparison of mass activity and price activity of all samples normalized to the Ru/Pt loading at the overpotential of 0.05 V vs. RHE. The TRO/RKLTO achieves a mass activity of 320 A g^{-1}_{Ru}, which is 68 times higher than that of commercial RuO_2 catalyst (4.7 A g^{-1}_{Ru}), and 1.7 times higher than Pt/C catalyst (193 A g^{-1}_{Pt}). With respect to the price activity (Supplementary Table 4), TRO/RKLTO (39 A $dollar^{-1}$) is 67 and 5.5 times higher than RuO_2 (0.58 A $dollar^{-1}$) and Pt/C (7 A $dollar^{-1}$), respectively. The HER activity of TRO/RKLTO is also far superior to those of transition metal oxides reported to date (Fig. 3f and Supplementary Table 5). It is also worthwhile to note that TRO/RKLTO exhibits much better mass activity than those of excellent Ru/Pt-relevant electrocatalysts, demonstrating its high electrocatalytic activity towards HER (Fig. 3f).[47-51]

Catalytic stability is another key criterion to evaluate the HER catalysts. The chronopotentiometry measurement shows that commercial RuO_2 displays a large performance decrease in the first ~5 h, and then maintains stable performance during the next 20 h (Supplementary Fig. 28). This situation is largely associated with structural changes on RuO_2, involving the transformation to ruthenium oxyhydroxide ($RuO(OH)_2$) and further reduction to metallic Ru.[52, 53] With regards to commercial Pt/C, the large increase of overpotential during the stability test stems from the aggregation or the detachment of Pt moieties from the carbon support.[54, 55] In sharp contrast, TRO/RKLTO only has a neglectable potential loss during the whole 25 h test (Supplementary Fig. 28). The XRD pattern demonstrates that there is no obvious peak shift or phase transformation of TRO/RKLTO after the durability test, implying the bulk structure of the KLTO substrate is well retained under alkaline test conditions (Supplementary Fig. 29).

To further confirm the stability of the TRO/RKLTO electrocatalyst under HER condition, we detected the metal dissolution amounts in the electrolyte by ICP-OES analysis. The results show that only ca. 0.02 ppm of Ru and ca. 0.05 ppm Ti can be detected in the electrolyte, which is negligible compared to those of used Ru and Ti elements in the electrode. This demonstrates the TRO/RKLTO is extremely stable under the HER working condition, possibly ascribed to the strong combination between TRO nanoparticles and KLTO perovskite oxide substrate. The used TRO/RKLTO was collected for XPS analysis, showing that the valence states of Ru and Ti have no obvious change without the formation of metallic Ru (280 eV) and $RuO(OH)_2$ (289 eV) after stability test (Supplementary Fig. 30).[53] The high-resolution XPS spectra of O 1s suggested that there was large amount of adsorbed H_2O (532 eV) after HER measurement. The EELS mapping for TRO/RKLTO after the long-term stability test shows no obvious phase segregation in the nanoparticle (Supplementary Fig. 31). In this approach, the incorporation of Ti could effectively suppress the excessive transformation of RuO_2 during the HER, and the strong interaction between the KLTO substrate and TRO nanoparticles could further stabilize the nanoparticles from aggregation.

Theoretical understanding of electrocatalytic activity for HER

To better understand the excellent performance of TRO/KLTO, we performed comprehensive calculations toward the HER process. Here different models (Fig. 4a and 4b) for Ru-doped KLTO and Ti-doped RuO_2 were built to study the adsorption behaviour on exposed surfaces. The (100) surface of KLTO and (110) surface of RuO_2, while considering the different terminations, were selected in our theoretical investigation as these two surfaces are the most commonly observed in both experiments and other simulations.[56] As discussed above, Volmer-Tafel mechanism is determined for KLTO/TRO as hydrogen adsorbates control the thermodynamic process. The Gibbs free energy for hydrogen adsorption (ΔG_{H^*}) is calculated following the standard procedure proposed by Nørskov et al.[35] In pure KLTO, the calculated free energies are either too positive or too negative for all metal sites and O-terminated sites (Fig. 4c), far away from the ideal "zero" value and correlating well to its poor HER performance. Once Ru is substituted into the KLTO lattice, the adsorption free energy changes differently over various doping sites. While negligible changes of free energy are found for Ru at both Ti and La sites, the nearly ideal value of -0.023 eV is obtained at the

Energy & Environmental Science

ARTICLE

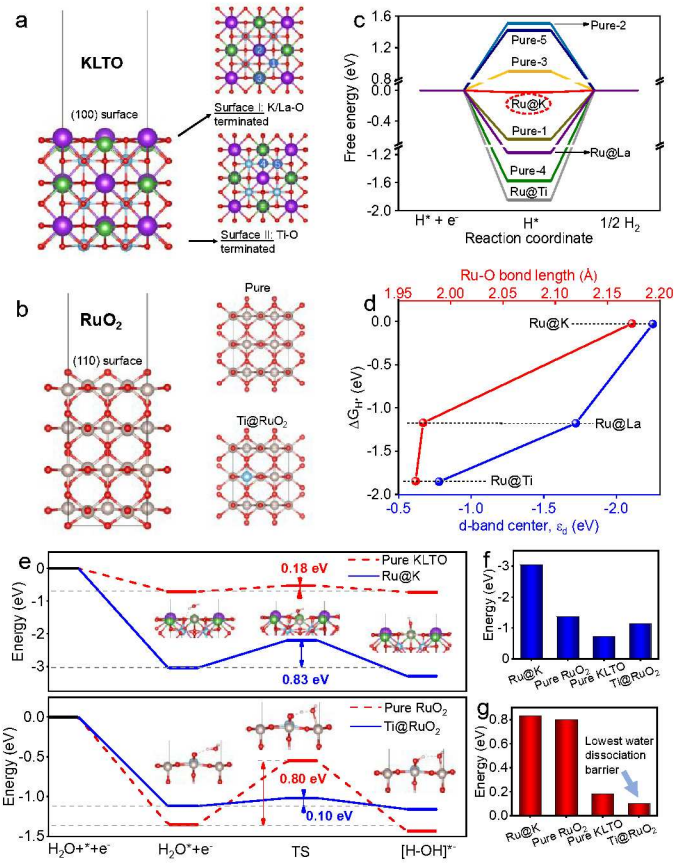

Fig. 4 DFT calculation. Models constructed for (a) (100) surface of KLTO and (b) (110) surface of RuO_2 in DFT calculations. Purple, green, blue, hazel and red atoms represent K, La, Ti, Ru and O atoms, respectively. c, Calculated free energy diagram of hydrogen evolution for pristine and doped KLTO. Thereinto, Ru replacing K site (Ru@K) is demonstrated to be the most active site with the lowest hydrogen adsorption free energy (in red dashed circle) d, Relationship between free energy and d-band center as well as Ru-O bond length. e, Energy diagrams for water adsorption and dissociation on the surfaces of KLTO (upper) and RuO_2 (lower). The adsorption energies of H_2O (f) and water dissociation barrier (g) on pure KLTO, Ru@K in KLTO, pure RuO_2 and Ti-doped RuO_2 (Ti@RuO_2).

most thermodynamically stable Ru@K site, indicating the substantial improvement of HER performance for Ru-doped KLTO. As seen from Fig. 4d, the ΔG_{H^*} increases with the d-band center downshifts and Ru–O bond length increases, which was also found in other calculations.[51, 57] The Ru-O bond length observed in our optimized structure of Ru-doped KLTO is 2.16 Å, which is larger than other reports thus corresponding to a minimum value of free energy. And for the RuO_2 system, the adsorption free energy is -0.88 eV at the bridging O site (Supplementary Fig. 32), in good agreement with other calculations.[51] However, the value is too negative to benefit the HER. After the substitution of Ti cation, the free energies are reduced by ~0.1 eV since the Ru-O bonds change negligibly, which is even worse for the ideal HER. Therefore, the hydrogen adsorption step is believed to be accelerated by the Ru-doping in KLTO rather than surface TRO nanoparticles.

Beside the thermodynamic process of H adsorption, the ability of water to dissociate under alkaline condition is more critical to HER because it is the sole approach to produce protons. This kinetic step can be evaluated by the energy barrier of $H_2O \rightarrow H^+ + OH^-$ on the surfaces using CI-NEB method to search for the transition state.[36] As shown in Fig. 4e and 4f, the strong binding to water of Ti@RuO_2 (-1.12 eV) system indicates that it can capture water molecules at a fast rate facilitating the Volmer process. The calculated barrier for H_2O on pure KLTO surface is 0.18 eV (Fig. 4e and 4g), which is quite low but the following H adsorption is not preferred as discussed above. And the energy barrier is even increased to 0.83 eV after the introduction of Ru into the stable K site of KLTO, making the kinetic

Energy & Environmental Science

ARTICLE

process more difficult. In contrast, the original energy barrier for pure RuO_2 is 0.80 eV (Fig. 4e and 4g) which is consistent with other calculations.[58] Once Ti is doped into the lattice of RuO_2, the energy barrier reduces remarkably to 0.10 eV (Fig. 4e and 4g) contributing to the easier water splitting and thus enhancing the HER performance.

Based on our theoretical findings, it can be concluded that the synergistic effect between Ru-doped KLTO (RKLTO) and Ti-doped RuO_2 (TRO) leads to significantly improved HER performance compared to pure KLTO. It should be noted the Ru-KLTO and Ti-doped RuO_2 clearly play the different roles in improving the HER performance. As the first step, the anchoring Ti-doped RuO_2 nanoparticles facilitate the dissociation of water molecules to obtain more hydrogen adsorbates. Further the adsorption of these H is tuned to the nearly ideal state on the Ru@K doped KLTO surface to finally contribute to the excellent HER performance via the Volmer-Tafel mechanism.

Conclusions

In summary, we have developed an efficient strategy for surface decoration of perovskites oxide via ion exchange and nucleation growth leading to highly active oxide-based electrocatalysts for alkaline HER. Under hydrothermal conditions, the ion exchange leads to the incorporation of Ru into the surface of KLTO, and nucleation growth produces Ti-doped RuO_2 nanoparticles on the surface. The resulting TRO/RKLTO showed the excellent activity for HER, superior to other oxide-based electrocatalysts and commercial Pt/C. The theoretical calculations indicate that incorporation of Ru into the surface of KLTO perovskite oxide is crucial in optimizing the hydrogen adsorption energy, and the doping of Ti to RuO_2 facilitates water dissociation. Thus, the synergy of TRO and RKLTO results in significantly promoted HER performance in alkaline solution. The present study demonstrates the potential of perovskite oxide in the field of alkaline HER, and opens a new direction for designing oxide-based catalysts with great capacity in energy conversion and storage.

Conflicts of interest

There are no conflicts to declare.

Acknowledgements

The authors are grateful to the financial support from Science and Technology Commission of Shanghai Municipality (16DZ2260603) and Equipment Research Program (6140721050215). J.W. thanks the program of Shanghai Academic Research Leader (20XD1424300) for financial support. J.H. and K.S. acknowledge the support from JST Research Acceleration Programme and JSPS-KAKENHI (JP16H06333). MRCAT operations are supported by the Department of Energy and the MRCAT member institutions. This research used resources of the Advanced Photon Source, a U.S. Department of Energy (DOE) Office of Science User Facility operated for the DOE Office of Science by Argonne National Laboratory under Contract No. DE-AC02-06CH11357.

Notes and references

1. J. Hwang, Z. Feng, N. Charles, X. R. Wang, D. Lee, K. A. Stoerzinger, S. Muy, R. R. Rao, D. Lee, R. Jacobs, D. Morgan and Y. Shao-Horn, *Mater. Today*, 2019, **31**, 100-118.
2. J. O. Bockris and T. Otagawa, *J. Electrochem. Soc.*, 1984, **131**, 290-302.
3. J. Suntivich, K. J. May, H. A. Gasteiger, J. B. Goodenough and Y. Shao-Horn, *Science*, 2011, **334**, 1383-1385.
4. M. A. Pena and J. L. Fierro, *Chem. Rev.*, 2001, **101**, 1981-2017.
5. J. P. Smit, P. C. Stair and K. R. Poeppelmeier, *Chem. Eur. J.* , 2006, **12**, 5944-5953.
6. R. P. Forslund, W. G. Hardin, X. Rong, A. M. Abakumov, D. Filimonov, C. T. Alexander, J. T. Mefford, H. Iyer, A. M. Kolpak, K. P. Johnston and K. J. Stevenson, *Nat. Commun.*, 2018, **9**, 3150.
7. H. Zhu, P. Zhang and S. Dai, *ACS Catal.*, 2015, **5**, 6370-6385.
8. J. Bak, H. Bin Bae and S. Y. Chung, *Nat. Commun.*, 2019, **10**, 2713.
9. J. D. Baniecki, H. Yamaguchi, C. Harnagea, D. Ricinschi, Z. Gu, J. E. Spanier, T. Yamazaki and H. Aso, *Adv. Energy Mater.*, 2019, **9**, 1803846.
10. Y. Chen, H. Li, J. Wang, Y. Du, S. Xi, Y. Sun, M. Sherburne, J. W. Ager, 3rd, A. C. Fisher and Z. J. Xu, *Nat. Commun.*, 2019, **10**, 572.
11. B. Hua, M. Li, Y. Zhang, Y. Sun and J. Luo, *Adv. Energy Mater.*, 2017, **7**, 1700666.
12. B. J. Kim, E. Fabbri, D. F. Abbott, X. Cheng, A. H. Clark, M. Nachtegaal, M. Borlaf, I. E. Castelli, T. Graule and T. J. Schmidt, *J. Am. Chem. Soc.*, 2019, **141**, 5231-5240.
13. N. K. Oh, C. Kim, J. Lee, O. Kwon, Y. Choi, G. Y. Jung, H. Y. Lim, S. K. Kwak, G. Kim and H. Park, *Nat. Commun.*, 2019, **10**, 1723.
14. M. Retuerto, L. Pascual, F. Calle-Vallejo, P. Ferrer, D. Gianolio, A. G. Pereira, A. Garcia, J. Torrero, M. T. Fernandez-Diaz, P. Bencok, M. A. Pena, J. L. G. Fierro and S. Rojas, *Nat. Commun.*, 2019, **10**, 2041.
15. X. Liu, L. Zhang, Y. Zheng, Z. Guo, Y. Zhu, H. Chen, F. Li, P. Liu, B. Yu, X. Wang, J. Liu, Y. Chen and M. Liu, *Adv. Sci.*, 2019, **6**, 1801898.
16. Y. Zhu, L. Zhang, B. Zhao, H. Chen, X. Liu, R. Zhao, X. Wang, J. Liu, Y. Chen and M. Liu, *Adv. Funct. Mater.*, 2019, **29**, 1901783.

17. J. Liu, E. Jia, L. Wang, K. A. Stoerzinger, H. Zhou, C. S. Tang, X. Yin, X. He, E. Bousquet, M. E. Bowden, A. T. S. Wee, S. A. Chambers and Y. Du, *Adv. Sci.*, 2019, **6**, 1901073.
18. F. Calle-Vallejo, N. G. Inoglu, H. Su, J. I. Martínez, I. C. Man, M. T. M. Koper, J. R. Kitchin and J. Rossmeisl, *Chem. Sci.*, 2013, **4**, 1245-1249.
19. J. Suntivich, W. T. Hong, Y. L. Lee, J. M. Rondinelli, W. Yang, J. B. Goodenough, B. Dabrowski, J. W. Freeland and Y. Shao-Horn, *J. Phys. Chem. C* 2014, **118**, 1856-1863.
20. W. T. Hong, K. A. Stoerzinger, Y. L. Lee, L. Giordano, A. Grimaud, A. M. Johnson, J. Hwang, E. J. Crumlin, W. Yang and Y. Shao-Horn, *Energ. Environ. Sci.*, 2017, **10**, 2190-2200.
21. M. Gong, W. Zhou, M. C. Tsai, J. Zhou, M. Guan, M. C. Lin, B. Zhang, Y. Hu, D. Y. Wang, J. Yang, S. J. Pennycook, B. J. Hwang and H. Dai, *Nat. Commun.*, 2014, **5**, 4695.
22. N. Spataru, J. G. LeHelloco and R. Durand, *J. Appl. Electrocchem.*, 1996, **26**, 397-402.
23. E. R. KOTZ and S. STUCKI, *J. Appl. Electrocchem.*, 1987, **17**, 1190-1197.
24. D. Guan, J. Zhou, Y. C. Huang, C. L. Dong, J. Q. Wang, W. Zhou and Z. Shao, *Nat. Commun.*, 2019, **10**, 3755.
25. T. Ling, D. Yan, H. Wang, Y. Jiao, Z. Hu, Y. Zheng, L. Zheng, J. Mao, H. Liu, X. Du, M. Jaroniec and S. Qiao, *Nat. Commun.*, 2017, **8**, 1509.
26. X. Xu, Y. Chen, W. Zhou, Z. Zhu, C. Su, M. Liu and Z. Shao, *Adv. Mater.*, 2016, **28**, 6442-6448.
27. Y. Zhu, W. Zhou, Y. Zhong, Y. Bu, X. Chen, Q. Zhong, M. Liu and Z. Shao, *Adv. Energy Mater.*, 2017, **7**, 1602122.
28. W. Zhao, G. Zhu, W. Zhao, T. Lin, F. Xu and F. Huang, *Dalton Trans.*, 2015, **44**, 18665-18670.
29. B. Ravel and M. Newville, *J. Synchrotron Rad.*, 2005, **12**, 537-541.
30. M. Newville, *J. Synchrotron Rad.*, 2001, **8**, 322-324.
31. G. Kresse and J. Furthmuller, *Phys. Rev. B*, 1996, **54**, 11169-11186.
32. P. E. Blochl, *Phys. Rev. B*, 1994, **50**, 17953-17979.
33. J. P. Perdew, K. Burke and M. Ernzerhof, *Phys. Rev. Lett.*, 1996, **77**, 3865-3868.
34. S. Grimme, J. Antony, S. Ehrlich and H. Krieg, *J. Chem. Phys.*, 2010, **132**, 154104.
35. J. K. Nørskov, T. Bligaard, A. Logadottir, J. R. Kitchin, J. G. Chen, S. Pandelov and U. Stimming, *J. Electrochem. Soc.*, 2005, **152**, J23-J26.
36. G. Henkelman, B. P. Uberuaga and H. Jónsson, *J. Chem. Phys.*, 2000, **113**, 9901-9904.
37. M. Sathiya, G. Rousse, K. Ramesha, C. P. Laisa, H. Vezin, M. T. Sougrati, M. L. Doublet, D. Foix, D. Gonbeau, W. Walker, A. S. Prakash, M. Ben Hassine, L. Dupont and J. M. Tarascon, *Nat. Mater.*, 2013, **12**, 827-835.
38. S. Nong, W. Dong, J. Yin, B. Dong, Y. Lu, X. Yuan, X. Wang, K. Bu, M. Chen, S. Jiang, L. Liu, M. Sui and F. Huang, *J. Am. Chem. Soc.*, 2018, **140**, 5719-5727.
39. S. Grimme, *J. Comput. Chem.*, 2006, **27**, 1787-1799.
40. R. Subbaraman, D. Tripkovic, K. C. Chang, D. Strmcnik, A. P. Paulikas, P. Hirunsit, M. Chan, J. Greeley, V. Stamenkovic and N. M. Markovic, *Nat. Mater.*, 2012, **11**, 550-557.
41. D. Strmcnik, P. P. Lopes, B. Genorio, V. R. Stamenkovic and N. M. Markovic, *Nano Energy*, 2016, **29**, 29-36.
42. D. Liu, X. Li, S. Chen, H. Yan, C. Wang, C. Wu, Y. A. Haleem, S. Duan, J. L. Lu, B. Ge, P. M. Ajayan, Y. Luo, J. Jiang and L. Song, *Nat. Energy*, 2019, **4**, 512-518.
43. Y. Jiao, Y. Zheng, K. Davey and S. Qiao, *Nat. Energy*, 2016, **1**, 16130.
44. Y. Zheng, Y. Jiao, A. Vasileff and S. Qiao, *Angew. Chem. Int. Ed.*, 2018, **57**, 7568-7579.
45. J. Wang, F. Xu, H. Jin, Y. Chen and Y. Wang, *Adv. Mater.*, 2017, **29**, 1605838.
46. R. Miao, B. Dutta, S. Sahoo, J. He, W. Zhong, S. A. Cetegen, T. Jiang, S. P. Alpay and S. L. Suib, *J. Am. Chem. Soc.*, 2017, **139**, 13604-13607.
47. J. Liu, Y. Zheng, Y. Jiao, Z. Wang, Z. Lu, A. Vasileff and S. Z. Qiao, *Small*, 2018, **14**, e1704073.
48. C. Wang and L. Qi, *Angew. Chem. Int. Ed.*, 2020, DOI: 10.1002/anie.202005436.
49. K. Yang, P. Xu, Z. Lin, Y. Yang, P. Jiang, C. Wang, S. Liu, S. Gong, L. Hu and Q. Chen, *Small*, 2018, **14**, e1803009.
50. X. Zheng, P. Cui, Y. Qian, G. Zhao, X. Zheng, X. Xu, Z. Cheng, Y. Liu, S. X. Dou and W. Sun, *Angew. Chem. Int. Ed.*, 2020, DOI: 10.1002/anie.202005241.
51. Y. Zhu, H. A. Tahini, Z. Hu, J. Dai, Y. Chen, H. Sun, W. Zhou, M. Liu, S. C. Smith, H. Wang and Z. Shao, *Nat. Commun.*, 2019, **10**, 149.
52. L. Å. Näslund, Á. S. Ingason, S. Holmin and J. Rosen, *J. Phys. Chem. C*, 2014, **118**, 15315-15323.
53. R. K. B. Karlsson, A. Cornell and L. G. M. Pettersson, *J. Phys. Chem. C*, 2016, **120**, 7094-7102.
54. D. Merki and X. Hu, *Energ. Environ. Sci.*, 2011, **4**, 3878-3888.
55. Z. Pu, I. S. Amiinu, Z. Kou, W. Li and S. Mu, *Angew. Chem. Int. Ed.*, 2017, **56**, 11559-11564.
56. K. A. Stoerzinger, L. Qiao, M. D. Biegalski and Y. Shao-Horn, *J. Phys. Chem. Lett.*, 2014, **5**, 1636-1641.
57. F. Y. Yu, Z. L. Lang, L. Y. Yin, K. Feng, Y. J. Xia, H. Q. Tan, H. T. Zhu, J. Zhong, Z. H. Kang and Y. G. Li, *Nat. Commun.*, 2020, **11**, 490.
58. Y. Fang and Z. Liu, *J. Am. Chem. Soc.*, 2010, **132**, 18214-18222.

Hydrogen (H_2) has been considered as an efficient energy carrier, standing out for its merits of high energy density and environmental sustainability. In recent years, electrocatalytic water splitting has become a promising approach to produce clean H_2. As a half-reaction of water splitting, hydrogen evolution reaction (HER) plays an important role, for which platinum (Pt) is the optimal electrocatalyst. Despite recent developments in non-Pt catalysts, few researches are relevant to transition metal oxide-based catalysts, which are generally inactive towards HER. Herein, we prepared a perovskite oxide-type electrocatalyst *via* surface ion exchanging with Ru cations and nucleation growth of Ti-doped RuO_2 (TRO) nanoparticles by facile hydrothermal treatment. The resultant oxide composite shows a remarkable HER activity with an ultra-low overpotential of 20 mV vs. RHE (@10 mA cm^{-2}), and a high mass (320 A g_{Ru}^{-1} @50 mV overpotential) and price activity (39 A $dollar^{-1}$ @50 mV overpotential), much superior to other oxide electrocatalysts and commercial Pt/C in alkaline condition. Theoretical simulation reveals the oxide surface plays the important bi-functional roles in alkaline HER. The TRO nanoparticles boost water dissociation and the Ru-ion-exchanged oxide surface facilitates hydrogen evolution. The synergistic strategy can be extended to other oxide-based electrocatalysts for the HER.